LETTER | MAY 24 2023

Near-field spectroscopy of Dirac plasmons in Bi_2Se_3 ribbon arrays

Lucy L. Hale ✉; Zhengtianye Wang; C. Thomas Harris; ... et. al

APL Photonics 8, 051304 (2023)
https://doi.org/10.1063/5.0135867

Near-field spectroscopy of Dirac plasmons in Bi_2Se_3 ribbon arrays

Cite as: APL Photon. 8, 051304 (2023); doi: 10.1063/5.0135867
Submitted: 23 November 2022 • Accepted: 8 May 2023 •
Published Online: 24 May 2023

Lucy L. Hale,[1,a] Zhengtianye Wang,[2] C. Thomas Harris,[3,4] Igal Brener,[3,4] Stephanie Law,[2,5] and Oleg Mitrofanov[1,3]

AFFILIATIONS

[1] University College London, Electronic and Electrical Engineering, London WC1E 7JE, United Kingdom
[2] Department of Materials Science and Engineering, University of Delaware, Newark, Delaware 19716, USA
[3] Center for Integrated Nanotechnologies, Sandia National Laboratories, Albuquerque, New Mexico 87123, USA
[4] Sandia National Laboratories, Albuquerque, New Mexico 87123, USA
[5] Materials Science and Engineering, Pennsylvania State University, University Park, Pennsylvania 16802, USA

[a] **Author to whom correspondence should be addressed:** lucy.hale@ucl.ac.uk

ABSTRACT

Plasmons supported in the massless electron surface states of topological insulators (TIs), known as Dirac plasmons, have great potential in next generation optoelectronics. However, their inherent confinement to the surface makes the investigation of Dirac plasmons challenging. Near-field techniques provide the ideal platform to directly probe Dirac plasmons due to the sensitivity to evanescent fields at the surface. Here, we demonstrate the use of aperture near-field spectroscopy for the investigation of localized terahertz (THz) Dirac plasmon resonances in Bi_2Se_3 ribbon arrays with widths ranging from 10 to 40 μm. Unlike scattering THz near-field techniques, the aperture method is most sensitive to plasmons with the relevant lower-momenta corresponding to plasmon wavelengths on the scale of ~20 μm. The combination of THz time-domain spectroscopy and aperture near-field microscopy enables sampling of localized Dirac plasmons in the near-field zone in the 0.5–2.5 THz range. We map the plasmon dispersion, which reveals a coupled plasmon–phonon polariton interaction. The near-field spectra show a higher contrast of the upper polariton branch in comparison with far-field observations. The information revealed by aperture near-field spectroscopy could deepen our understanding of the behavior of Dirac plasmons, leading to the potential development of real-world TI devices.

INTRODUCTION

Topological insulators (TIs) are a class of materials that are insulating in the bulk but conductive on the surface owing to topologically protected, two-dimensional metallic surface states.[1–3] TIs include Bi_2Se_3, Sb_2Te_3, Bi_2Te_3, and their compounds. Electrons existing in the topological surface states are massless and exhibit spin–momentum locking, in which the electron momentum determines its spin state. This unique property of the surface states prevents electrons from backscattering into other surface states and makes TIs highly attractive materials for fundamental studies as well as for future applications in high-speed dissipationless electronics, spintronic devices,[4,5] and quantum computing.[3,6]

One route to using TIs in next generation optoelectronic devices is through plasmonics. Plasmons in metals and semiconductors have proved extremely useful for sensing, photodetection, and imaging applications due to their strong field confinement and high sensitivity to refractive index changes.[7–10] At terahertz (THz) frequencies, where many fundamental low-energy excitations exist, plasmonics is a particularly attractive tool for waveguiding and coupling THz waves to matter in a range of sensing applications.[11–13] Plasmons supported in the topological surface states of TIs, known as Dirac plasmons, are of even further scientific interest due to their unique spin-polarized nature[4] and tunable Fermi level through doping,[14,15] which opens the door to even broader potential applications.[16–19] Of all the known TIs, Bi_2Se_3 is an

ideal candidate for the study of Dirac plasmons, as it has the largest bandgap, lowest carrier density, and no alloy scattering.[20,21]

While Dirac plasmons could offer a whole host of useful functionalities, previous spectroscopic investigations of Bi_2Se_3 have revealed a very complex optoelectronic behavior, and it remains a challenge to detect and isolate the Dirac plasmons from other contributions arising from the bulk states.[21–24] One of the technical difficulties in studying Dirac plasmons in Bi_2Se_3 is their high in-plane momenta, which are much larger than the free space momenta. At THz frequencies, the momenta of Dirac plasmons are $>10^3$ cm^{-1},[25] corresponding to wavelengths on the micrometer scale. This means that exfoliated flakes and individual subwavelength resonators supporting plasmons in Bi_2Se_3 are practically invisible for far-field spectroscopy. Consequently, large arrays of subwavelength sized ribbons, which can couple a plane wave excitation to localized plasmon resonances, have been used to investigate Dirac plasmons in the far-field.[25–29] Alternatively, direct probing of highly confined Dirac plasmons is possible using near-field methods. By enabling the investigation of subwavelength-size isolated resonators, near-field techniques could provide crucial knowledge of Dirac plasmons in TIs, including the spatial distribution, mode profiles, and spectroscopic information.

So far, attempts to study Dirac plasmons in the near-field have been performed with scattering-type near-field microscopy (s-SNOM).[22,23] This technique uses a sharp metallic tip to launch plasmon waves, which then reflect at a material defect, such as an edge, return to the tip, and scatter back to the far-field [Fig. 1(b)].[30,31] However, due to the sub-micrometer size of the scattering tip and its tapping motion, the s-SNOM method is most sensitive to plasmons with even higher in-plane momenta, $>10^5$ cm^{-1}, and has been used to detect hyperbolic phonon–plasmon polaritons in Bi_2Se_3 [Fig. 1(c)].[23] The near-field s-SNOM detection of the fundamental plasmons, characterized by smaller momenta ($\lambda \sim 20$ μm), has proved extremely challenging: the lower sensitivity of s-SNOM at these momenta makes it very difficult to map the spatial distribution of strongly damped plasmons and necessitates the use of elaborate analysis to extract the plasmon properties.[22]

Here, we use an alternative near-field method called aperture near-field microscopy (a-SNOM) to study surface plasmons in Bi_2Se_3. This method uses a subwavelength size aperture to locally detect evanescent THz fields within several micrometers from the sample surface [Fig. 1(a)]. The aperture method, which has previously been used to study plasmons in metals and graphene,[32–35] is different from the scattering-type method in several key aspects. First, rather than launching plasmons using a sharp tip, the sample can be uniformly illuminated from the far-field, allowing direct excitation of plasmonic resonances (for example, at ribbon edges). The THz field near the sample surface is then probed with minimal invasion with micrometer-level spatial resolution. Second, the aperture probe does not restrict the probing of plasmons with low values of in-plane momenta in contrast to scattering-type microscopy. Figure 1(c) shows the normalized spectral sensitivity of a 10 μm aperture probe compared to scattering tips of different radii. While the scattering probes have a peak sensitivity at a momentum determined by the tip radius, the aperture probe does not have a lower momentum cutoff, allowing the measurements of fundamental THz plasmons with wavelengths on the order of 10–100s of micrometers. In this study, the aperture near-field method is also combined with time-domain spectroscopy (TDS), which enables measurements of temporal evolution of plasmon excitation and covers a spectrum of 0.5–2.5 THz—a range where previous investigations had limited sensitivity.[22,23]

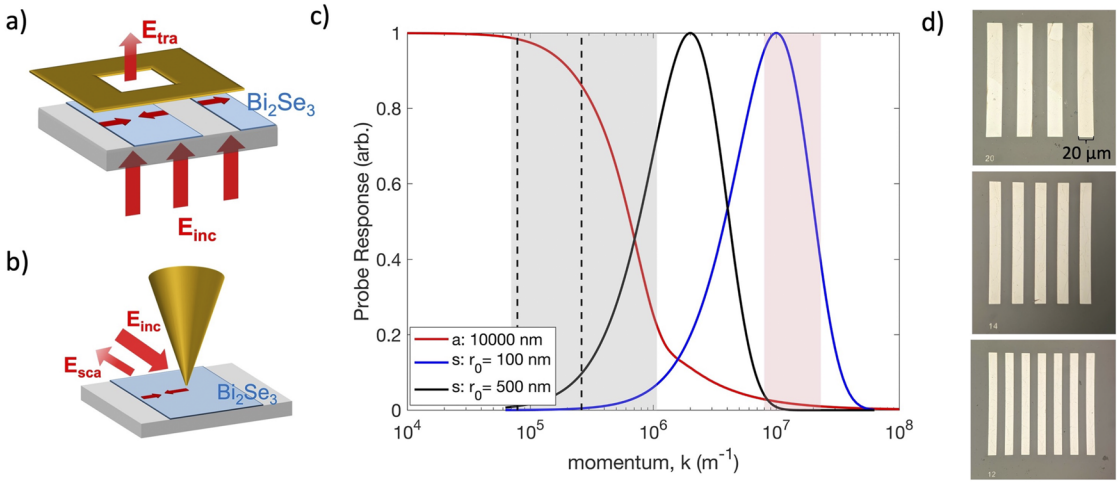

FIG. 1. Comparison of near-field techniques for probing surface plasmons. (a) Schematic showing normal incidence excitation of surface plasmons in ribbon structures and aperture-probe detection scheme. (b) Schematic showing excitation and detection of surface plasmons using the scattering tip scheme. (c) Normalized probe response for a 10 μm aperture (red), compared to scattering probes with a 100 nm (blue) and 500 nm (black) tip radius. The shaded areas represent the in-plane momenta of the fundamental Bi_2Se_3 Dirac plasmons measured from ribbon arrays in Refs. 25 and 26 and the present study (gray) ($1–30 \times 10^3$ cm^{-1}) and hyperbolic plasmons measured in Ref. 23 (pink) ($0.8–1.5 \times 10^5$ cm^{-1}). The dashed lines indicate the largest and smallest momenta probed in the present study. The probe sensitivity evaluation is presented in the supplementary material. (d) Microscope image of ribbon arrays (ribbon widths: 20, 14, and 12 μm).

We investigate thin-film Bi_2Se_3 ribbon arrays and observe localized plasmon resonances in the spectral region close to the phonon frequency. By experimentally mapping the plasmon dispersion and comparing to analytical and numerical models of Dirac plasmons, we conclude that the observed spectral signature originates from Dirac plasmons coupled to the Bi_2Se_3 phonon near 2 THz. We also compare the near-field and far-field measurements, which sheds light on the different near-field visibility of the upper and lower polaritons. We find that the aperture SNOM is a complementary technique to s-SNOM and far-field methods for investigating TIs, and it can be used to form a full picture of plasmon excitations in these materials, which is crucial for translating TI material research into real device development.

METHODS

The Bi_2Se_3 samples in this study were 100 nm thick and grown by molecular beam epitaxy (MBE) on a 0.5 mm thick sapphire substrate.[36–38] Sapphire is commonly used as a substrate for TI growth due to its high resistivity and, therefore, high transparency at THz frequencies. The Bi_2Se_3 thickness is deeply subwavelength so that the material is in the thin-film limit,[25] where plasmons on the top and bottom surfaces are coupled. Moreover, thicknesses over 100 nm could also lead to a greater contribution from the bulk conductivity, which can mask the Dirac plasmons. Please see the supplementary material for further analysis of the Bi_2Se_3 thickness. The measured mobility of electrons in the Bi_2Se_3 films was $\mu_m \approx 843\ cm^2\ V^{-1}\ s^{-1}$.

To excite plasmons, the Bi_2Se_3 layer was patterned using photolithography into ribbon arrays of varying ribbon width, W, and a period of $2W$. The ribbon arrays, which have previously been used to study Dirac plasmons in Bi_2Se_3 in the far-field,[25–28] as well as in other 2D materials, such as graphene,[35,39–42] enable momentum matching and, therefore, coupling of the incident plane wave to surface plasmons. The momentum of excited surface plasmons is defined by W as $q = \pi/W$. An example of the simulated electric field distribution around a Bi_2Se_3 ribbon can be seen in the supplementary material—the electric field is concentrated at the ribbon edges and there are significant field components polarized out of the ribbon plane.

A schematic of the aperture near-field measurement is shown in Fig. 1(a). The entire sample area is illuminated by a broadband THz plane wave emitted from an InAs source. A THz detector with a 10 μm input aperture is placed a few micrometers from the sample, allowing us to probe the THz field near the sample surface with a spatial resolution of ~10 μm.[43] The source and near-field probe are excited by femtosecond IR pulses in a standard time domain spectroscopy (TDS) configuration, enabling sampling of the THz field in time and the full retrieval of THz field amplitude and phase. In addition, by scanning the sample across the probe, the THz field across the surface of the entire sample can be mapped.

For a comparison to the near-field spectra, we also characterized THz transmission in larger area ribbon samples using a quasi-far-field spectroscopy setup [Figs. 2(a) and 2(b)], where the aperture probe is replaced with a standard photoconductive antenna detector positioned several millimeters from the sample surface. The rest of the experimental setup, including the source and sample position, remained the same as for the near-field measurements.

RESULTS

We first examine the far-field transmission spectra of ribbon arrays of different ribbon widths (12 and 40 μm, Fig. 2). Ribbon arrays were measured in both TE (dashed lines) and TM (solid lines) orientations and were normalized to the incident field spectrum. In

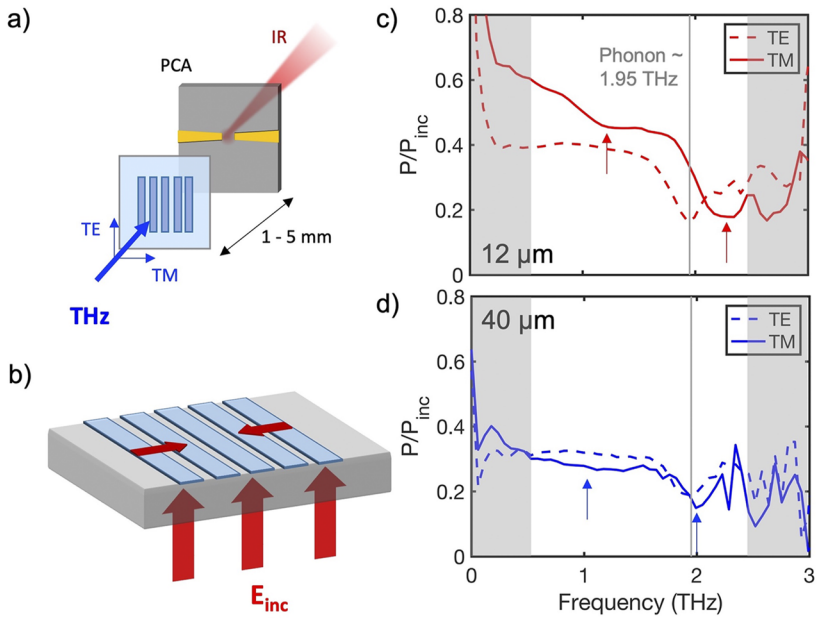

FIG. 2. (a) Schematic of the far-field measurement setup (b) Schematic of plasmon excitation: the incident field is scattered by the edges of the ribbons to launch plasmons. (c) and (d) Measurement of 12 μm (c) and 40 μm (d) ribbon arrays with TE and TM polarized light. The gray line indicates the frequency of the Bi_2Se_3 α phonon.

the TE case, we observe a distinct dip in transmission just below 2 THz for both ribbon arrays. This is expected due to the presence of the α phonon in Bi_2Se_3 at a frequency of 1.95 THz.[44] However, for the TM polarized measurements, this dip appears to be slightly shifted to higher frequencies for the 40 μm ribbon array and more substantially shifted for the 12 μm ribbon array. In addition, the TM spectra also show a broader, less prominent dip in transmission for both arrays at lower frequencies around 1 THz, which is not present in the TE case.

The modification of the phonon spectra around 2 THz suggests a coupling of the α phonon to another nearby resonance. The coupling is only present for TM polarized light when localized plasmon modes can be directly excited in the ribbons, suggesting that the phonon is coupled to a plasmon resonance. This phenomenon has been observed previously in far-field measurements of Bi_2Se_3 ribbon arrays.[25,45] Furthermore, the increase in the frequency of the transmission dips with decreasing ribbon width is consistent with the spectral signature from Dirac plasmons, where the plasmon frequency is expected to scale inversely with $\sqrt{W}$,[26] as will be discussed later.

Having confirmed plasmon–phonon coupling in Bi_2Se_3 ribbon arrays in the far-field, we then analyzed small patches ($150 \times 150\ \mu m^2$) of ribbon arrays using the aperture probe. Because the probe detects the electric field directly at the surface, it can detect evanescent fields of the plasmons that are not directly accessible in the far-field. Figure 3(a) shows a space–time map of the THz field across a sample with three ribbon gratings (TM polarization) for ribbon widths W = 14, 16, and 20 μm. There are three distinct darker regions on the plot (white arrows), which correspond to the positions of the three ribbon arrays, indicating that the THz waveform is modified in these regions. Near-field spectra for each of the ribbon arrays were obtained by a Fourier transform of the waveforms from the array center. Interestingly, all the ribbon arrays enhance the THz transmission through the sample compared to the bare substrate. This effect, which has also been seen previously in graphene and TI ribbon arrays,[26,35] is attributed to impedance matching by the Bi_2Se_3 array at the sapphire–air interface. To account for the reflection loss in the reference sapphire spectrum, the amplitude of the spectrum was scaled such that it matches that of the ribbon arrays in the low-frequency region. The Bi_2Se_3 ribbon spectra were then normalized to this substrate-only spectra (Ref), making any spectral difference between the Bi_2Se_3 and reference clearer [Fig. 3(b)]. In Fig. 3(c), the normalized spectra can be seen for arrays with ribbon widths spanning from 12 to 20 μm.

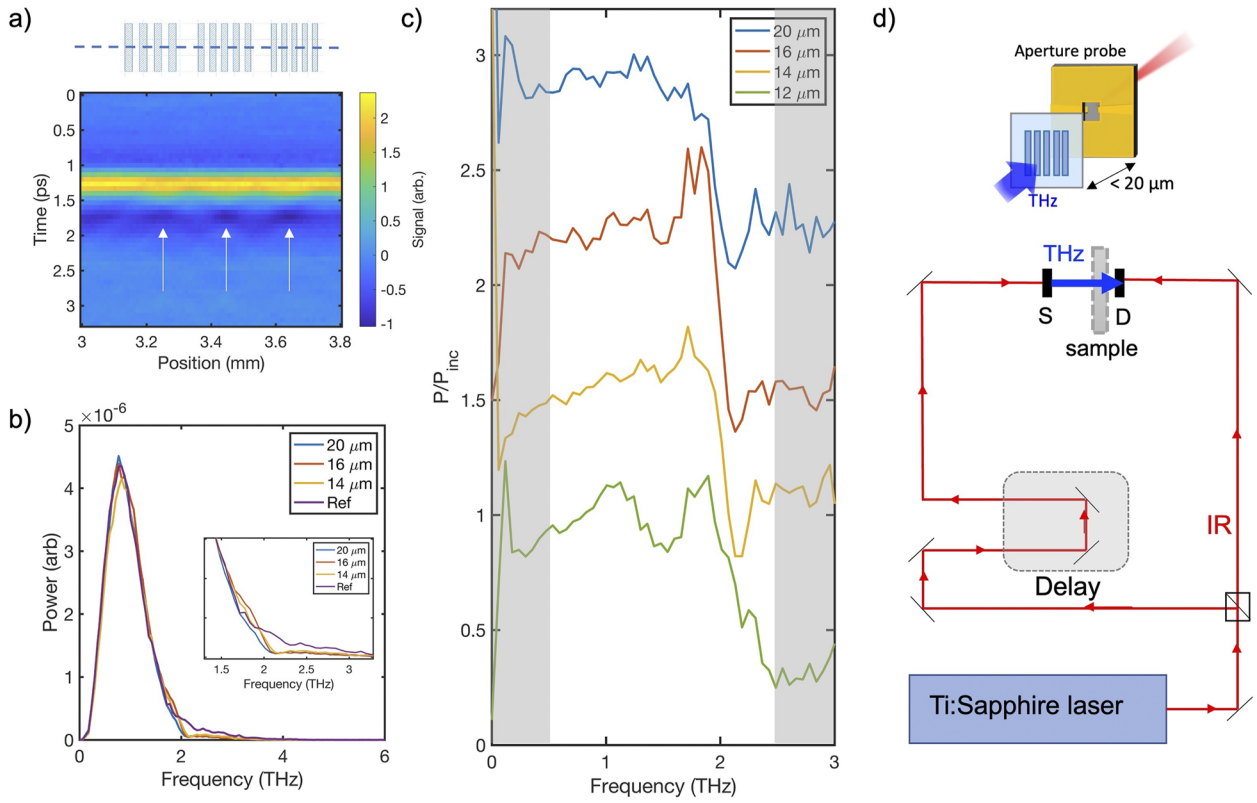

FIG. 3. Near-field spectroscopy of Bi_2Se_3 ribbon arrays. (a) Space–time map across three ribbon arrays. Each vertical slice corresponds to waveform in time measured at a point on the dashed line. (b) Spectra measured on 14, 16, and 20 μm ribbon arrays, compared to substrate-only spectra. The inset shows the close-up on the region of spectra where the ribbon spectra are significantly modified. (c) Spectra of 12, 14, 16, and 20 μm ribbon arrays spaced apart for clarity, normalized to the substrate-only spectra [shown in (b)]. (d) Schematic of the aperture near-field TDS setup, with a close-up of the sample and detector configuration.

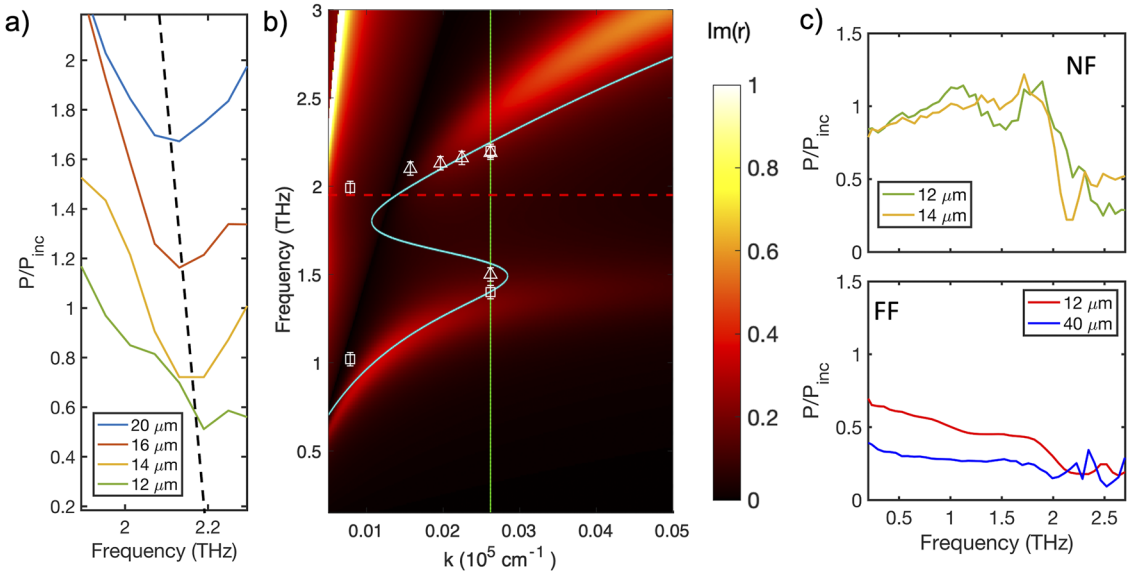

FIG. 4. Dispersion analysis: (a) Close-up of the normalized near-field spectra, showing shift in transmission dip frequency with ribbon width. (b) Dispersion relation of coupled phonon–Dirac plasmons, calculated using the transfer matrix method [imaginary part of reflection coefficient, Im(r)] and analytical model (turquoise line). Data points overlaid show the resonant frequencies extracted from near-field (white triangles) and far-field (white squares) data. The error bars represent the spectral resolution of the measurement. The green line indicates plasmon momentum for a 12 μm ribbon array. (c) Comparison of near-field (NF) spectra (top panel) to far-field (FF) spectra (lower panel).

In all the near-field spectra, a very abrupt drop in transmission is seen near 2 THz, showing a relatively narrow dip with some recovery at higher frequencies. The dip is slightly shifted to higher frequencies in comparison with the bare α-phonon resonance (1.95 THz). On closer inspection, the frequency of the transmission minima varies with the ribbon width [Fig. 4(a)] similarly to the far-field spectra. However, compared to the far-field spectra, the contrast between the high and low transmission levels is significantly higher (>70%).

It is difficult to identify clear spectral signatures in the region below 2 THz with the exception of the 12 μm array, which shows a broad drop in transmission at 1.5 THz. The absence of clear spectral features at lower frequencies compared to the far-field measurements could be due to a poor signal-to-noise ratio, given that the spectral features observed at these frequencies in the far-field are considerably less pronounced and broader than the features at higher frequencies. We also note that the near-field signal contains several contributions in addition to the localized surface fields, of which all superimpose, leading to potential enhancement or suppression of spectroscopic features.[46]

DISCUSSION

The dependence of the spectral peak near 2 THz on W in both the near- and far-field spectra, combined with the presence of two distinct peaks in the far-field, indicates an interaction between the α-phonon and plasmon supported by the Bi_2Se_3 ribbons. To confirm this effect and determine the origin of the plasmon wave—surface or bulk—we compared the observed peaks in Figs. 2 and 3 to theoretical dispersion models of a Dirac plasmon–phonon interaction. The polariton in-plane momentum was defined by the ribbon width, and the dispersion of the α phonon coupled to Dirac plasmons was calculated analytically using Eq. (1),[25]

$$\omega^2_{plasmon} = \frac{e^2}{\varepsilon_0}\frac{v_F\sqrt{2\pi n_{2D}}}{h}\frac{q}{\varepsilon_1+\varepsilon_2+q\,d\varepsilon_3}, \tag{1}$$

where q is the plasmon momentum; d is the Bi_2Se_3 layer thickness; ε_1, ε_2, and ε_3 are the permittivities of the top (air), bottom (sapphire), and middle (Bi_2Se_3) dielectric layers; $v_F = 5\times10^5$ m/s is the Fermi velocity; and $n_{2D} = 1.2\times10^{13}$ cm^{-2} is the 2D sheet carrier concentration. The 2D sheet carrier density is calculated using Hall measurements assuming that most carriers exist in the surface states. The permittivity of Bi_2Se_3 is modeled using FTIR reflectance measurements. Further information about the Bi_2Se_3 permittivity and the analytical calculation can be found in Ref. 25.

The analytical calculation results are shown by the turquoise line in Fig. 4(b) overlaid on a color map displaying absorption due to coupled Dirac plasmon–phonon polaritons, which is calculated numerically using a transfer matrix method (TMM). In the TMM calculations, the electromagnetic field on one side of the Bi_2Se_3 layer is related to the field on the other side through transfer and propagation matrices, and the topological surface states are treated as infinitesimally thin layers with finite conductivity. The imaginary part of the reflection coefficient Im(r) is extracted, which indicates the losses in the system. This TMM is discussed extensively in Refs. 45, 47, and 48 and has been used to accurately reproduce the experimentally measured dispersion of both single- and multilayer Bi_2Se_3 structures. All the parameters in the TMM are the same with

those adopted in Eq. (1), with an extra parameter for the carrier relaxation time, $\tau = 1$ ps.

In the analytical model, a kink appears due to the coupling of the plasmon with the α phonon at 1.95 THz, whereas in the TMM color plot an anti-crossing behavior can be seen around the phonon frequency, where the spectral feature is split in two. This signifies the coupling of the excited plasmons to the phonon, resulting in upper and lower polariton branches.

The frequencies of the upper and lower polariton branches measured in the experimental data were plotted by selecting the center of each dip in transmission by sight [Fig. 4(b), white markers]. The error bars represent the frequency resolution of the measurement system. In the experimental far-field data (white squares), the two spectral features observed for each ribbon array agree well with the frequencies of the upper and lower polariton branches of the TMM model. We note that there is additional uncertainty associated with the choice of spectral frequency for the lower polariton branch, which is not very pronounced. In addition, although the lower polariton branch is not always visible in the near-field data (white triangles), the frequencies of the spectral features agree well with the upper polariton frequencies predicted by the TMM matrix model and overlap with the analytical calculation. We therefore conclude that the spectral signature reveals the coupling of plasmons excited in the topological surface state to the phonon, and the formation of Dirac plasmon–phonon polaritons. Due to the poor visibility of the lower polariton branch, it is difficult to precisely determine the experimental coupling strength. However, using the near-field spectra for the 12 and 14 μm ribbon arrays, we can estimate a splitting of ~0.6 THz. It is possible that some of the carriers are bulk carriers or they exist in 2DEG states at the surface rather than the topological surface state. However, the expected spectral response for coupling between the phonon and 2DEG plasmon or phonon and bulk carrier plasmon do not match our data, as has been discussed previously in Refs. 22, 25, and 45. The best agreement is found when assuming all carriers are in the topological surface states.

Finally, Fig. 4(c) highlights the potential of the aperture near-field technique for probing Dirac plasmons in resonant Bi_2Se_3 structures compared to standard far-field techniques. While both the far- and near-field measurements display a change in transmission above the 2 THz resonance, it is significantly more pronounced in the near-field. The combination of aperture near-field microscopy with THz-TDS is the only near-field method that has enabled broadband spectroscopy of TI ribbon arrays so far, as previous s-SNOM were conducted at select THz frequencies and are limited in bandwidth by the frequency of the source.

CONCLUSION

In conclusion, we have observed plasmon–phonon polaritons in Bi_2Se_3 ribbon arrays using aperture near-field spectroscopy. The broadband TDS technique allowed us to map the dispersion of plasmons near the phonon resonance in the material. We rigorously analyzed the experimental spectra by comparing them to analytical and numerical models and confirm that the plasmon–phonon polariton originates from the topological surface state. The near-field spectra also revealed a higher contrast of the upper polariton branch in comparison with far-field observations. Due to the spatial resolution on the micrometer scale and sensitivity to plasmons with an in-plane momentum around 10^3 cm^{-1}, the aperture SNOM combined with THz-TDS is an ideal technique for investigating TIs, and it is complementary to the scattering-type SNOM and far-field methods. Aperture-type near-field spectroscopy can be further utilized to map mode profiles on TI-based waveguides and individual subwavelength resonators, providing vital information for the development of useful topological insulator devices.

SUPPLEMENTARY MATERIAL

See supplementary material for information of the probe sensitivity calculations, material growth and nanofabrication.

ACKNOWLEDGMENTS

This work was supported by the U.S. Department of Energy, Office of Basic Energy Sciences, Division of Materials Sciences and Engineering. L.L.H. was supported by the EPSRC (Grant Nos. EP/P021859/1, EP/L015455/1, and EP/T517793/1). Z.W. and S.L. acknowledge the funding from the U.S. Department of Energy, Office of Science, Office of Basic Energy Sciences, under Award No. DE-SC0017801. Far-field experiments were performed at the Center for Integrated Nanotechnologies, an Office of Science User Facility operated for the U.S. Department of Energy (DOE) Office of Science. Sandia National Laboratories is a multimission laboratory managed and operated by National Technology and Engineering Solutions of Sandia, LLC., a wholly owned subsidiary of Honeywell International, Inc., for the U.S. Department of Energy's National Nuclear Security Administration under Contract No. DE-NA-0003525. This article describes objective technical results and analysis. The views expressed in the article do not necessarily represent the views of the U.S. DOE or the United States Government. The authors thank Doug Pete for assisting with thickness characterization of Bi_2Se_3 using AFM.

AUTHOR DECLARATIONS

Conflict of Interest

The authors have no conflicts to disclose.

Author Contributions

Lucy L. Hale: Formal analysis (lead); Investigation (equal); Writing – original draft (lead). **Zhengtianye Wang**: Data curation (equal); Formal analysis (supporting); Investigation (supporting); Visualization (supporting); Writing – review & editing (supporting). **C. Thomas Harris**: Investigation (supporting); Resources (supporting); Writing – review & editing (supporting). **Igal Brener**: Funding acquisition (equal); Resources (equal); Writing – review & editing (supporting). **Stephanie Law**: Conceptualization (equal); Funding acquisition (supporting); Investigation (supporting); Resources (supporting); Supervision (supporting). **Oleg Mitrofanov**: Conceptualization (equal); Formal analysis (supporting); Investigation (equal); Methodology (lead); Supervision (equal); Writing – original draft (supporting); Writing – review & editing (supporting).

DATA AVAILABILITY

The data that support the findings of this study are available from the corresponding author upon reasonable request.

REFERENCES

[1] H. Zhang, C.-X. Liu, X.-L. Qi, X. Dai, Z. Fang, and S.-C. Zhang, Nat. Phys. **5**, 438 (2009).
[2] M. Z. Hasan and J. E. Moore, Annu. Rev. Condens. Matter Phys. **2**, 55 (2011).
[3] J. E. Moore, Nature **464**, 194 (2010).
[4] D. Pesin and A. H. MacDonald, Nat. Mater. **11**, 409 (2012).
[5] I. Vobornik, U. Manju, J. Fujii, F. Borgatti, P. Torelli, D. Krizmancic, Y. S. Hor, R. J. Cava, and G. Panaccione, Nano Lett. **11**, 4079 (2011).
[6] H. P. Paudel and M. N. Leuenberger, Phys. Rev. B **88**, 085316 (2013).
[7] E. Ozbay, Science **311**, 189 (2006).
[8] M. Kauranen and A. v. Zayats, Nat. Photonics **6**, 737 (2012).
[9] S. A. Maier, *Plasmonics: Fundamentals and Applications* (Springer, 2007).
[10] M. S. Tame, K. R. McEnery, Ş. K. Özdemir, J. Lee, S. A. Maier, and M. S. Kim, Nat. Phys. **9**, 329 (2013).
[11] X. Zhang, Q. Xu, L. Xia, Y. Li, J. Gu, Z. Tian, C. Ouyang, J. Han, and W. Zhang, Adv. Photonics **2**, 1 (2020).
[12] M. Dragoman and D. Dragoman, Prog. Quantum Electron. **32**, 1–41 (2008).
[13] D. M. Mittleman, Nat. Photonics **7**, 666 (2013).
[14] T. Zhang, J. Ha, N. Levy, Y. Kuk, and J. Stroscio, Phys. Rev. Lett. **111**, 056803 (2013).
[15] Y. L. Chen, J. G. Analytis, J. Chu, Z. K. Liu, S. Mo, X. L. Qi, H. J. Zhang, D. H. Lu, X. Dai, Z. Fang, S. C. Zhang, I. R. Fisher, Z. Hussain, and Z. Shen, Science **325**, 178 (2009).
[16] T. Stauber, J. Phys.: Condens. Matter **26**, 123201 (2014).
[17] A. Politano, L. Viti, and M. S. Vitiello, APL Mater. **5**, 035504 (2017).
[18] Y. P. Lai, I. T. Lin, K. H. Wu, and J. M. Liu, Nanomater. Nanotechnol. **4** (2014).
[19] T. Ginley, Y. Wang, Z. Wang, and S. Law, MRS Commun. **8**, 782 (2018).
[20] Y. Xia, D. Qian, D. Hsieh, L. Wray, A. Pal, H. Lin, A. Bansil, D. Grauer, Y. S. Hor, R. J. Cava, and M. Z. Hasan, Nat. Phys. **5**, 398 (2009).
[21] A. Politano, V. M. Silkin, I. A. Nechaev, M. S. Vitiello, L. Viti, Z. S. Aliev, M. B. Babanly, G. Chiarello, P. M. Echenique, and E. v. Chulkov, Phys. Rev. Lett. **115**, 216802 (2015).
[22] S. Chen, A. Bylinkin, Z. Wang, M. Schnell, G. Chandan, P. Li, A. Y. Nikitin, S. Law, and R. Hillenbrand, Nat. Commun. **13**, 1374 (2022).
[23] E. A. A. Pogna, L. Viti, A. Politano, M. Brambilla, G. Scamarcio, and M. S. Vitiello, Nat. Commun. **12**, 6672 (2021).
[24] Y. Deshko, L. Krusin-Elbaum, V. Menon, A. Khanikaev, and J. Trevino, Opt. Express **24**, 7398 (2016).
[25] T. P. Ginley and S. Law, Adv. Opt. Mater. **6**, 1800113 (2018).
[26] P. di Pietro, M. Ortolani, O. Limaj, A. di Gaspare, V. Giliberti, F. Giorgianni, M. Brahlek, N. Bansal, N. Koirala, S. Oh, P. Calvani, and S. Lupi, Nat. Nanotechnol. **8**, 556 (2013).
[27] S. Nasir, Z. Wang, S. v. Mambakkam, and S. Law, Appl. Phys. Lett. **119**, 201103 (2021).
[28] M. Autore, H. Engelkamp, F. D'Apuzzo, A. D. Gaspare, P. D. Pietro, I. L. Vecchio, M. Brahlek, N. Koirala, S. Oh, and S. Lupi, ACS Photonics **2**, 1231 (2015).
[29] P. di Pietro, N. Adhlakha, F. Piccirilli, A. di Gaspare, J. Moon, S. Oh, S. di Mitri, S. Spampinati, A. Perucchi, and S. Lupi, Phys. Rev. Lett. **124**, 226403 (2020).
[30] F. Keilmann, J. Electron Microsc. **53**, 187–192 (2004).
[31] X. Chen, D. Hu, R. Mescall, G. You, D. N. Basov, Q. Dai, and M. Liu, Adv. Mater. **31**, 1804774 (2019).
[32] R. Mueckstein and O. Mitrofanov, Opt. Express **19**, 3212 (2011).
[33] O. Mitrofanov, Y. Todorov, D. Gacemi, A. Mottaghizadeh, C. Sirtori, I. Brener, and J. L. Reno, Opt. Express **26**, 7437 (2018).
[34] M. Natrella, O. Mitrofanov, R. Mueckstein, C. Graham, C. C. Renaud, and A. J. Seeds, Opt. Express **20**, 16023–16031 (2012).
[35] O. Mitrofanov, W. Yu, R. J. Thompson, Y. Jiang, Z. J. Greenberg, J. Palmer, I. Brener, W. Pan, C. Berger, W. A. de Heer, and Z. Jiang, Solid State Commun. **224**, 47 (2015).
[36] Y. Wang, T. P. Ginley, and S. Law, J. Vac. Sci. Technol., B: Nanotechnol. Microelectron.: Mater., Process., Meas., Phenom. **36**, 02D101 (2018).
[37] Z. Wang and S. Law, Cryst. Growth Des. **21**, 6752 (2021).
[38] T. P. Ginley and S. Law, J. Vac. Sci. Technol., B: Nanotechnol. Microelectron.: Mater., Process., Meas., Phenom. **34**, 02L105 (2016).
[39] Z. Fei, M. D. Goldflam, J. S. Wu, S. Dai, M. Wagner, A. S. McLeod, M. K. Liu, K. W. Post, S. Zhu, G. C. A. M. Janssen, M. M. Fogler, and D. N. Basov, Nano Lett. **15**, 8271 (2015).
[40] J. Chen, M. Badioli, P. Alonso-González, S. Thongrattanasiri, F. Huth, J. Osmond, M. Spasenović, A. Centeno, A. Pesquera, P. Godignon, A. Zurutuza Elorza, N. Camara, F. J. G. de Abajo, R. Hillenbrand, and F. H. L. Koppens, Nature **487**, 77 (2012).
[41] A. Y. Nikitin, F. Guinea, F. J. García-Vidal, and L. Martín-Moreno, Phys. Rev. B **84**, 161407 (2011).
[42] A. Y. Nikitin, F. Guinea, F. J. Garcia-Vidal, and L. Martin-Moreno, Phys. Rev. B **85**, 081405 (2012).
[43] L. L. Hale, J. Keller, T. Siday, R. I. Hermans, J. Haase, J. L. Reno, I. Brener, G. Scalari, J. Faist, and O. Mitrofanov, Laser Photonics Rev. **14**, 1900254 (2020).
[44] P. di Pietro, F. M. Vitucci, D. Nicoletti, L. Baldassarre, P. Calvani, R. Cava, Y. S. Hor, U. Schade, and S. Lupi, Phys. Rev. B **86**, 045439 (2012).
[45] Z. Wang, T. P. Ginley, S. V. Mambakkam, G. Chandan, Y. Zhang, C. Ni, and S. Law, Phys. Rev. Mater. **4**, 115202 (2020).
[46] O. Mitrofanov, Z. Han, F. Ding, S. I. Bozhevolnyi, I. Brener, and J. L. Reno, Appl. Phys. Lett. **110**, 061109 (2017).
[47] D. Q. To, Z. Wang, Y. Liu, W. Wu, M. B. Jungfleisch, J. Q. Xiao, J. M. O. Zide, S. Law, and M. F. Doty, Phys. Rev. Mater. **6**, 085201 (2022).
[48] D. Q. To, Z. Wang, D. Q. Ho, R. Hu, W. Acuna, Y. Liu, G. W. Bryant, A. Janotti, J. M. O. Zide, S. Law, and M. F. Doty, Phys. Rev. Mater. **6**, 035201 (2022).